Computationally guided synthesis of carbon coated mesoporous silica materials

Nabankur Dasgupta,[1#] Qian Mao,[2#] and Adri van Duin[2*]

[1]*Geochemistry Department, Sandia National Laboratories, Albuquerque, NM 87123*

[2]*Mechanical Engineering Department, The Pennsylvania State University, University Park, PA 16802*

# Equally contributed author

* Corresponding author: acv13@psu.edu

Abstract

Mesoporous silica materials (MSMs) have unique features like large surface area and tunable pore size, making them suitable for biomedical applications. For longer durability, the small pores in MSMs are kept intact by filling them with carbon precursors, which are carbonized to prevent them from interacting with unreacted silicic acid. In this study, we synthesize and heal MSMs using a combination of non-reactive and reactive molecular dynamics (MD) simulations. We use Pluronic® L64 polymers to form micelle assembly in water, which are interpreted from radial distribution function and hydrogen bonding networks of water molecules with the hydrophilic/hydrophobic segments of the polymers. Orthosilicic acid is condensed around the micelle-water assembly using bond-boosted ReaxFF MD simulations. Then, the system is calcinated to burn down the carbonaceous micelle structure with evaporation of water. Subsequently, we perform the healing of MSM surface by carbonizing polymer precursors inside an MSM pore. Polyethylene and lignite are rendered as the most suitable precursors due to their

ability to form a network of turbostratic graphene structures. To assess the performance of turbostratic graphene structure-based coatings on the inner surface of the MSM nanopore, we introduce silicic acid precursor inside the pore and monitor its movement.

1. Introduction

Mesoporous silica materials (MSMs) have gained tremendous success in various applications recently, mainly due to their interesting and unique textural and structural features. These features include high specific surface, pore volumes, and unique pore sizes, which allow their use in processes such as catalysis, adsorption, separation of target molecules, drug delivery devices, chemosensors, and biosensors [1,2]. They exhibit greater capacity for drugs loading and ensure a controlled bio-active compound release if they are functionalized, in comparison with amorphous colloidal silica [3]. They are usually prepared from the self-assembly of surfactants, such as pluronic polymers in solvents, followed by rapid condensation of silica precursors around the micelle. The silicate condenses and forms an outer shell around the self-assembly. The self-assembly along with the solvent is then calcinated at high temperature which induces pore in the system [4]. MSMs are prepared using either the cooperative template method [5], where the silicates play a crucial role during formation of the mesostructure; or the liquid crystal templating mechanism [6], where the structure of preformed surfactant liquid crystals determines the MSM structure, while silicates simply condense around these preformed mesophases. The composition and type of the surfactants, auxiliary chemicals, and the synthetic condition allows us to monitor the desirable pore size, wall thickness, and pore shape. Understanding and controlling interfacial interactions, association, and aggregation is vital to the goal-oriented use of MSMs. There are several MSMs which have been reported in the past two decades [7]: MCM-41, MCM-48, SBA-15 and SBA-16.

Functionalization of ordered MSMs has been extensively studied over the years in an effort to provide appropriate properties for specific applications [3]. Functionalization serves several diverse purposes such as: (1) Enhancing the properties of the inner surface for better adsorption-reaction processes [8–14], (2) Acting as an anti-corrosion agent to protect inner surface of mesopores [15–21], and (3) serving as enhanced controlled drug release purposes [22–27]. Functionalization in the form of grafting leads to co-condensation of carbon precursors with the silica of the inner pores, which can significantly alter the pore properties [12] leading to better adsorption of gases. Carbon precursors can also act as corrosion inhibitors for hundreds of industrial applications [15]. Polymeric coatings on materials provide a dense barrier against corrosive species [16]. Types of coatings which serve the purpose of anticorrosion agents are: (1) polymeric or sol-gel coatings [28,29]; (2) silane based coatings [30,31]; (3) carbon based coatings [32,33]; and (4) smart nanocontainers [34,35], which, when dispersed into the system, can quickly respond to the local environmental changes associated with changes in pH and ionic strength. Corrosion inhibitors in the form of polymers are generally immobilized or encapsulated inside polymeric micro-capsules and released inside meso- and nano-pores. These materials are required to be carbonized at high temperature to obtain the solid residue or the coating which settles and heals the inner surface of the mesopores [36].

In order to understand the formation mechanism and to develop new mesoporous materials, tremendous efforts have been made in experimental studies for the synthesis and functionalization of MSMs [5,20,37–42]. Although significant progress has been made in the experimental studies of the synthesis process of these materials, having a thorough understanding of the atomic structure, interactions, and formation mechanism is important. Due to the amorphous nature of atomic distribution in MSMs, it remains challenging for current experimental techniques to

provide detailed information about the atomic structures of silica mesopore walls. Atomistic simulations offer the potential to provide microscopic insights into the molecular level mechanism of the synthesis process. Simulating the formation of MSMs is a challenging task because of the simultaneous interplay between electrostatic interactions, hydrophobic forces, and condensation polymerization reactions. Building a molecular model which can capture all this broad range of effects of the synthesis process can be complicated. Furthermore, factors related to large system size and long-time scale simulations are required to observe self-assembly and polymerization. As a result, there have been cases of molecular modeling reported to address these problems [43–48].

Early stages of MSM formation using molecular modeling encounter issues related to length and timescale. Methods such as kinetic Monte Carlo [49] and Monte Carlo using coarse grained lattice models [45,48,50] are some of the methods which have proven valuable for studying the synthesis process. Coarse grained molecular dynamics (MD) using MARTINI force field has been effective in reaching microseconds of simulations depicting the micelle self-assembly in the solution [51,52]. Non-reactive force fields such as OPLS-AA [53], CMAS94 [54], and CLAYFF [55] along with SPC/E or TIP3P water models [56] have been able to delineate the silica association within the solution effectively. Simple algorithms such as pore-drilling [57,58] and cylindrical resist [59,60] methods have been developed to create a silica nanopore, enabling MD simulations to bypass the micellization step. Recent developments of rather complex algorithms such as poreMS [61] have been productive in generating effective functionalized mesoporous silica structures for atomistic simulations. Despite the significant amount of computational work which has gone into the development of MSMs, there are limitations in understanding the atomic details and the formation pathway of phases at each step of the atomistic simulations. This is restricted by the

high complexity of the interactions and reactions occurring within the system along with the system size effects.

Reactive force fields such as ReaxFF [62,63] have been able to address and elucidate the behavior and dynamics of large complex chemical systems [64–68]. It can handle multi-atomic systems and predict the correct kinetics and reaction mechanism of the system. For large chemical systems, ReaxFF simulations are sometimes limited to a few nanoseconds due to the complexity of the interatomic potential functions. Accelerated algorithms have therefore been developed and utilized over the years in conjunction with MD simulations to study rare events [69–72]. Therefore, to investigate the synthesis and post synthesis healing of MSMs, we use a combination of non-reactive (OPLS-AA) and reactive (ReaxFF) force fields for our current study to process and analyze each step accordingly. We report the formation of self-assembly of pluronic polymer in water based on the interplay between the hydrophilic and hydrophobic parts of the polymer with water, followed by the silicic acid condensation at ambient temperature and final calcination of the carbonaceous self-assembly and water. The post synthesis healing of these materials is done by carbonizing carbon precursors – lignite, cellulose, polyethylene (PE), polyethylene terephthalate (PET), and sucrose inside the mesopores. We elucidate the functionality and behavior of each of these precursors based on the products formed from carbonization. Lastly, we discuss the ability of the carbonized precursors to block unreacted silicic acid from damaging the small pores during the synthesis of MSMs.

2. Simulation Details

We consider L64 ($PEO_{13}PPO_{30}PEO_{13}$) pluronic polymer as the basic unit for the formation of micelle in water. PEO stands for Polyethylene Oxide, which forms the hydrophilic tail, and PPO stands for Polypropylene Oxide, which forms the hydrophobic head. We performed atomistic MD

simulation for the self-assembly of pluronic polymers in solution on the GROningen MAchine for Chemical Simulations (GROMACS) [73] platform with the OPLS-AA force field. The initial configuration of the polymer molecules is assembled from the monomer units, called residues. The entire chain configuration was built by linking the residues along the z-direction. We used the pdb2gmx tool in GROMACS, which is designed to generate the topology files for proteins. For our system, we treat the linear block copolymer as a linear sequence of residues defined in the residue topology file aminoacids.rtp. pdb2gmx treats this linear sequence of residues as a protein sequence. New entries in the aminoacid.rtp file can generate molecule.itp files for any linear polymer consisting of a sequence of residues. We used the extended simple point charge model [74] (SPC/E) for water to solvate the pluronic polymers. This is a rigid 3-point water model with a polarization correction term.

For the self-assembly simulations, we utilized 20 L64 molecules in a system consisting of 5000 water molecules. We equilibrated the system by performing NVT simulations at 298.15 K after geometry energy minimization. We performed atomistic MD simulation for the self-assembly of pluronic polymers in water on the GROMACS platform. NPT production runs were performed using Nose-Hoover [75] thermostat at 298.15 K and a pressure of 1 bar by Parrinello-Rahman [76] barostat for 300 ns. The equations of motion were integrated using the leapfrog algorithm [77] with a timestep of 2 fs.

After obtaining self-assembly of the pluronic polymer in the solution, we extracted the final frame of the simulation. Then, we introduced 1000 molecules of orthosilicic acid within the system around the periphery of the micelle. For the healing simulations, we used the ReaxFF force field developed by Pitman et al. [78], which is provided in the Supplementary Information (SI) file. We minimized the system using the force field and then equilibrated it at 298.15 K with the NVT

ensemble. For the NVT simulations, we employed the Berendsen [79] thermostat with a timestep of 0.25 fs. To facilitate the condensation of the silica precursor around the self-assembly, we conducted an accelerated ReaxFF MD simulation for 2 ns with the bond-boosting framework [71,80]. The parameters for bond-boosting the system can be found in Table S1 of the SI file. Each cycle of bond-boosting lasted 3.75 fs. To test the temperature-dependent condensation rate, we performed sample simulations by placing 60 molecules of silicic acid in a box. The condensation of silicic acid was studied at two different temperatures: 300 K using a bond-boosting technique and 1500 K to observe the rate difference. After achieving an early stage of silica condensation around the polymer self-assembly, we proceeded to calcinate the system. This step involved subjecting the system to an extremely high temperature, causing disruption to the micelle structure. To illustrate the calcination process, we fixed the atoms of the micelle water system and allowed the condensed and unreacted orthosilicic acid to interact and form a condensed phase within the system. Subsequently, we heated the system from 298.15 K to 2000 K with a heating rate of 6.8 K/ps, followed by the calcination at this elevated temperature for 1 ns in the NVT ensemble.

To coat the mesopores of the MSMs, we constructed an amorphous silica nanoslab, which was annealed at 1500 K and subsequently quenched to 300 K. A cylinder with a diameter of 4 nm was carved along the *z*-direction of the amorphous silica nanoslab to create the mesopore. To account for missing protons from the dangling oxygen within the inner pore walls, we introduced 1000 water molecules into the pore. The system was then subjected to minimization and equilibration using the ReaxFF force field at 300 K for 100 ps. Next, we elevated the system temperature to 1400 K and equilibrated it using the NVT ensemble for 1 ns to establish hydrogen bonds with the dangling oxygen on the inner pore walls. This procedure closely resembled the cylindrical resist method described in reference [60]. The unreacted water molecules were removed from the

system, and it was quenched back to 300 K. We utilized this silica nanopore for performing the subsequent healing simulations using ReaxFF MD.

For the healing simulations, we considered five different polymer precursors: cellulose, lignite, polyethylene (PE), polyethylene terephthalate (PET), and sucrose. The number of molecules of polymers used for the carbonization process was determined by considering a density of 1 g/cm^3, which was calculated from the pore volume of the MSM. We minimized the geometries of polymers and then equilibrated the systems at 300 K using the NVT ensemble. The systems were heated from 300 K to 2200 K and 2600 K, with a heating rate of 3.8 K/ps and 4.6 K/ps respectively. Final carbonization simulations were then performed at these two temperatures for 1 ns to determine the optimal polymers as coating agents for the mesopores. For all the NVT simulations, we employed the Berendsen [79] thermostat with a timestep of 0.25 fs. To determine the effectiveness of these coatings as blocking agents, we introduced an unreacted silica precursor into the pore space. Subsequently, we conducted MD simulations for 100 ps to monitor the movement of the unreacted silicic acid within the pore.

All ReaxFF MD simulations were performed on the AMS platform [81]. In the subsequent sections, we delve into the synthesis and healing processes, drawing upon our simulation results for comprehensive analysis and discussion.

3. Results and Discussions

3.1.Self-assembly of polymers

We describe results of atomistic modeling of the early stages of the synthesis of MSMs using MD simulations. Explicit MD simulations of silica condensation are not feasible at the condition examined in this study due to the inability of the MD method to sample the timescales required for

the complete reaction to take place. The surfactant assembly usually takes a very long time to self-assemble compared to the silica condensation reactions. The NPT simulations for 200 ps first find small clusters of surfactant molecules which are scattered over the system. Then an Ostwald ripening process is followed leading to the formation of larger micelles. The initial stages of micelle formation are slow and the growth proceeds mostly by collision between micelles. A representation of the pluronic polymer containing a hydrophilic tail (green part of the polymer) and a hydrophobic head (red part of the polymer at the center) is shown in **Fig. 1**a, followed by the unit monomers of ethylene oxide (see **Fig. 1**b) and propylene oxide (see **Fig. 1**c) constituting the polymer. The large micelle formed at the end of the NPT simulation is shown in **Fig 2**a. The properties calculated for the self-assembly of polymers in water include the O-H pair radial distribution function (RDF) as well as the solvent distribution represented by hydrogen bond evolution, as depicted in **Fig. 2**b and **Fig. 2**c, respectively. To determine the hydrogen bond distribution, we employ a bond distance cutoff of 3.5 Å for the hydrogen bond donor and acceptor atoms, along with an angle cutoff of 100° for the donor-acceptor-acceptor antecedent angle ($\hat{H}$). **Fig. 2**b reveals that the hydrophilic segment of the pluronic polymer exhibits a stronger interaction with water in the solution compared with the hydrophobic segment, as evidenced by the higher intensity of the characteristic peak for ethylene oxide at r = 0.18 nm. As the simulation proceeds, ethylene oxide demonstrates an increasing number of hydrogen bonds, whereas propylene oxide exhibits a decreasing trend of hydrogen bonding, as seen in **Fig. 2**c. The quantification of hydrogen bonds serves as an indicator for solvent distribution in proximity to the polymers, revealing the affinity of water for ethylene oxide over propylene oxide. Our results indicate that the segregation of hydrophilic and hydrophobic segments is well obtained. Nearly 80 % of the hydrogen bonds are observed to form near the hydrophilic section of the micelle (see **Fig. 2**c). This phenomenon aligns

with previous observations seen in TEM images during the self-assembly of F127 pluronic polymers [82].

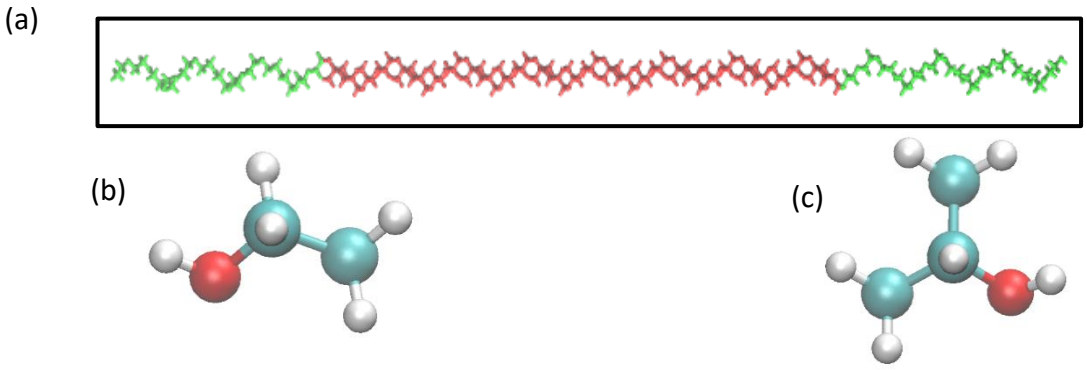

Figure 1: (a) Pluronic L64 polymer with its hydrophilic component in green (ethylene oxide) and its hydrophobic component in red (propylene oxide), (b) structure of ethylene oxide, and (c) structure of propylene oxide.

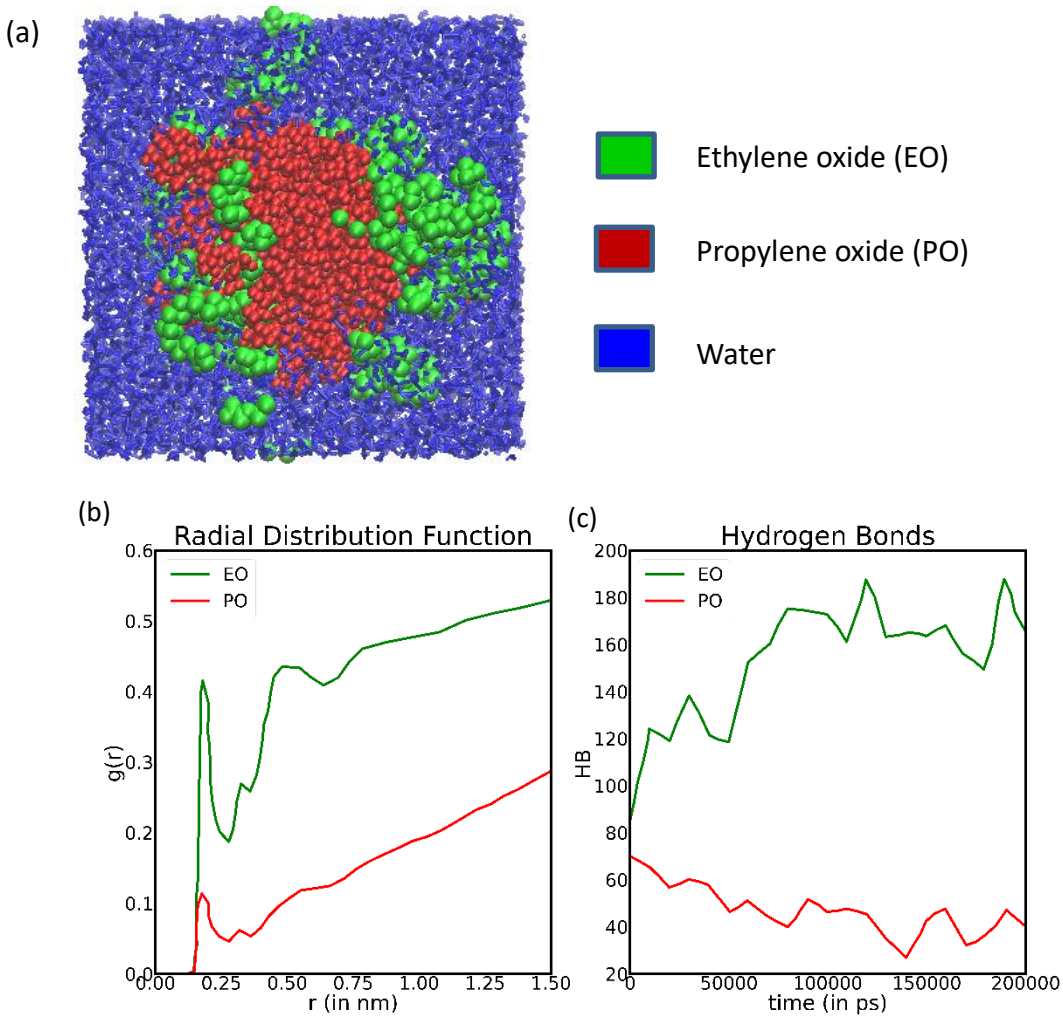

Figure 2: (a) Formation of self-assembly of pluronic polymer in water, (b) O-H pair radial distribution function (RDF) of hydrophilic and hydrophobic segments of pluronic polymer in water, and (c) hydrogen bond formation of hydrophilic and hydrophobic segments of pluronic polymer with water.

3.2.Effect of silica condensation

Once a micelle structure is formed, silica precursors in the form of orthosilicic acid are introduced at the periphery of the micelle-water system. Subsequently, a gradual condensation process allows them to bind and form a structure around the micelle. To parameterize the force constants of the

external potential, we optimize the activation energy barrier of the condensation reaction against benchmarked DFT barrier energy calculations [83]. The reason for using an optimized sets of force constant parameters is not to force the condensation reaction, which can damage the self-assembly in the process. The comparisons of the energies obtained for silicic acid dimerization and trimerization between ReaxFF and DFT are presented in **Fig. 3**, which suggests that the transformation is primarily influenced by the dimerization due to its lower activation energy.

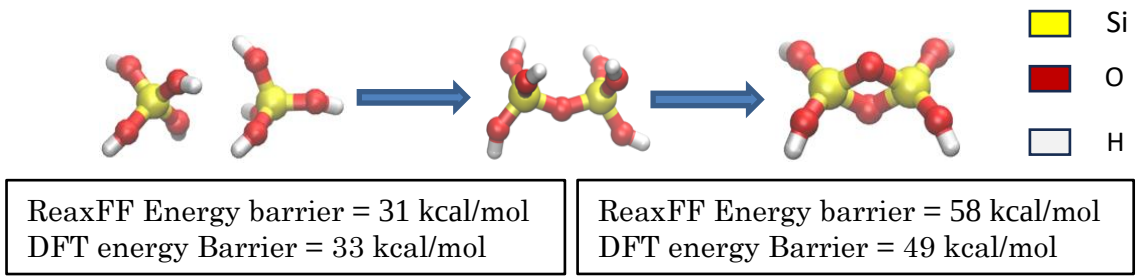

Figure 3: Comparisons of ReaxFF and DFT energy barriers for silicic acid dimerization and trimerization [83].

The association and agglomeration of silica precursors during the 2 ns simulation are outlined in **Fig. 4**. The condensation shows that not all dimerization or trimerization reactions of silicic acid are found to be successful in every cycle of bond-boosting. Consequently, some orthosilicic acid remains unreacted at the end of the simulation. Experimentally, the underlying kinetics may be balanced by the choice of solvent, colloid concentration, and by surfactant molecules to temporarily hinder the ripening of the silanol groups [84–86]. Once the condensed mesoporous phase of silica is obtained, we proceed to the final step, namely, the calcination of the carbonaceous micelle. When comparing simulations to experiments, an additional challenge arises such that the

former takes time to reach equilibrium. Simulations become trapped in a metastable state, and the resulting outcome mainly depends on the starting configuration. Applying bond-boosting in conjunction with molecular dynamics forces the atoms of interest to take part in the reaction once a pre-transition state is obtained. This allows the system to escape from the metastable state from being trapped. However, using abnormal values of force constants in bond-boosting might lead to potentially detrimental effect on the system yielding undesired products and unwanted dynamics of atoms. Therefore, optimized parameters needs to be obtained which yield the closest reaction energy barrier compared to DFT barrier [80] which should then be applied for studying chemical reactions in large systems.

Our results indicate the formation of condensed silica on the surface of the micelle (see **Fig. 4**b), followed by dehydration resulting in the creation of periodic mesoporous silica within the system (see **Fig. 4**d). This phenomenon aligns with the prior observation made by Jorge et al. [87] When around 60 % of the silica precursors condense around the self-assembly using bond-boosting, we proceed to calcinate the system at 2000 K.

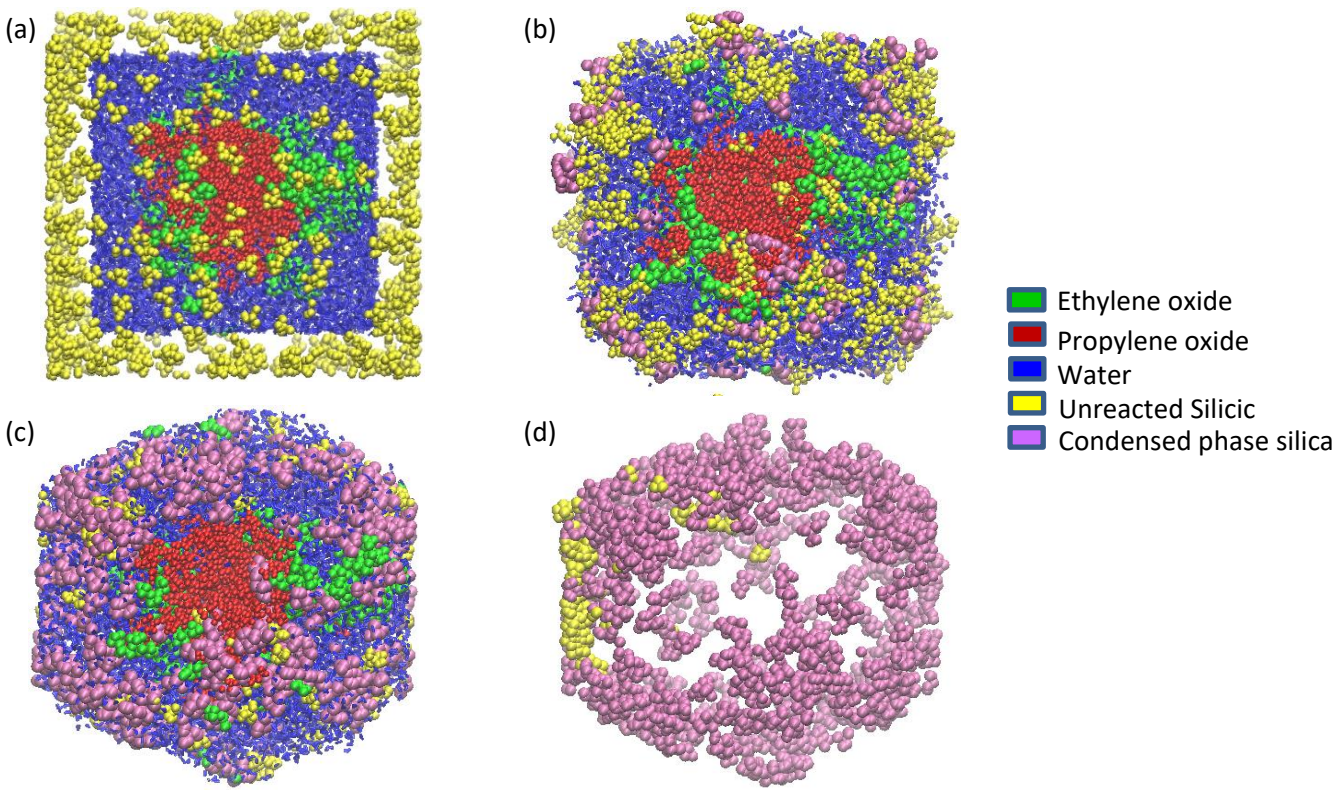

Figure 4: Molecular snapshots of (a) silica initial association around the self-assembly, (b) silica condensation on the surface of micelle-water system, (c) silica condensation augmenting with time, and (d) calcinating the system and removing the carbonaceous micelle and water from the system.

3.3.Calcination of micelle water self-assembly

The final step of the synthesis process requires the calcination of the carbonaceous matter from the system along with the evaporation of water. This keeps the mesoporous silica phase intact within the system, resulting in the formation of pores from the calcination process. One of the phenomena observed during the calcination process, which occurs at high temperature, is that silicic acid aggregates much faster compared to that at ambient temperature. This observation has been previously reported by both experimental studies [88] and simulations [89]. To substantiate this

hypothesis, we conduct a small-scale simulation focusing on $Si(OH)_4$ molecule condensation, as outlined in Section 2.

Fig. 5a represents the condensation rate of silicic acid at 300 K and 1500 K. **Fig. 5**a reveals that the dimerization rate of $Si(OH)_4$ at room temperature is 0.5/ps, and it remains relatively stable from 20 ps to 80 ps; while beyond 80 ps, it levels off and reaches a plateau. In contrast, for the high temperature condensation at 1500 K, we observe a dimerization rate close to 1/ps, which initiates around 20 ps and maintains stability until 80 ps. The computed condensation rate at 300 K with bond-boosting and at 1500 K without bond-boosting demonstrates that even in the absence of bond-boosting, high temperatures significantly promote the polymerization of $Si(OH)_4$, nearly doubling the rate (see **Fig. 5**a), compared to ambient temperature. However, as noted previously by Du et al. [89], the condensation of silicic acid increases only up to a specific temperature, which should also be below the glass transition temperature. Another interesting observation is that we find a small number of clusters of $Si(OH)_4$ agglomerating within the system at high temperature, which eventually dimerizes and creates a network. **Fig. 5**b displays a cluster showing agglomeration of silicic acid precursors condensing at 1500 K. For our current system, the network of condensed silica forms at 2000 K, as shown in **Fig. 4**d. Following the calcination process, the carbonaceous micelle burns down, accompanied by the evaporation of water molecules, which, in turn, induces the formation of pores. The final structure of the synthesized mesoporous silica is illustrated in **Fig. 4**d. These pores play a crucial role in enabling transport and diffusion processes of various molecules and substances, making these materials widely applicable.

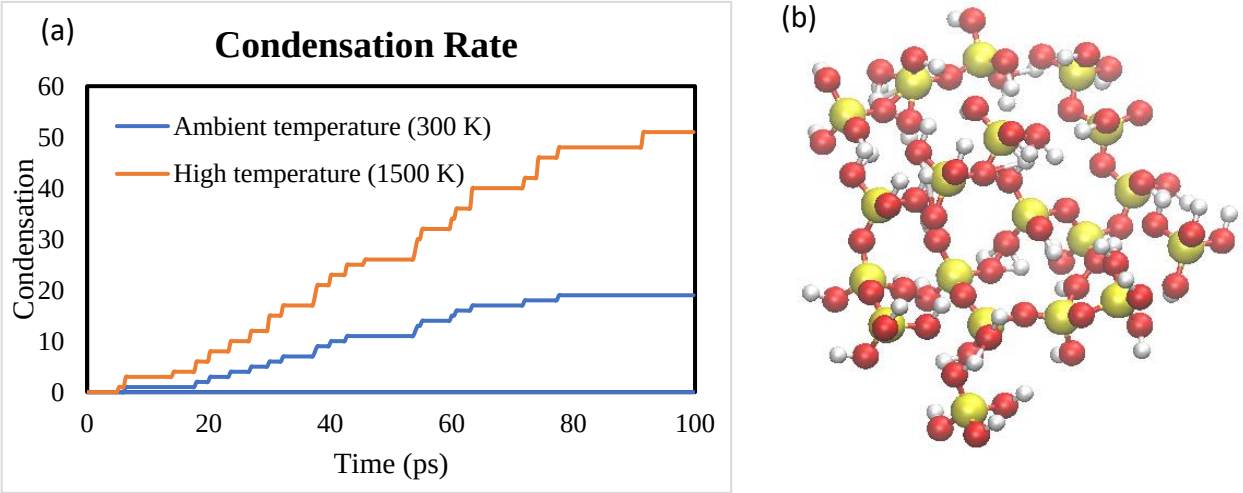

Figure 5: (a) Condensation of silicic acid at ambient and high temperature for a 100 ps simulation and (b) agglomeration of silicic acid forming rapidly at high temperature.

3.4.Carbon ring formation analysis

Following the synthesis of an MSM, we create a 4 nm diameter silica pore structure, as detailed in Section 2. Subsequently, we introduce various carbon precursors into this structure, as depicted in **Fig. 6**. The carbonization reaction of precursors proceeds rapidly at the target temperatures, 2200 K and 2600 K. To assess the degree of carbonization for various precursors, we record the 5 to 7-membered all-carbon rings at the two temperatures. Our analysis primarily centers on the formation of 6-membered all-carbon rings, as they predominantly correspond to sp^2 hybridized carbon structures within turbostratic graphene networks. The 5 and 7-membered rings, which are the unstable aromatic rings formed from topological defects, are also of interest in this study. These all-carbon rings (5, 6, 7-membered) account for more than 60 % of all-carbon atoms present in the polymer. The all-carbon rings of interest are normalized to a ratio that denotes the carbon atom conversion, with the unique number of carbon atoms forming the 5, 6, 7-membered all-carbon

rings divided by the total number of carbon atoms for each case. As discussed in the previous studies [90,91], we utilize the ratio instead of the percentage because the summation of the percentages of 5, 6, 7-membered all-carbon rings can exceed 100 %, due to the possibility of one carbon atom contributing to multiple types of all-carbon rings during carbonization.

Fig. S1 illustrates the absolute counts of 5, 6, and 7-membered rings formed during carbonization simulations conducted over 1 ns. The ratios of carbon atom conversion into 5, 6, and 7-membered all-carbon rings for each polymer precursor during carbonization are presented in **Fig. 7**. As depicted in **Fig. 7**, lignite exhibits the highest carbon conversion ratio to 6-membered rings among all the polymers, closely followed by PE. However, the precursors initially consist of 6-membered heteroatom rings, which, upon carbonization, produce fragments as predominant gaseous products. In comparison with 6-membered all-carbon rings, the conversion ratios to 5 and 7-membered all-carbon rings show a gradual increase for most of the polymers. After t = 0.2 ns, we observe a stabilization of 6-membered rings at 2600 K for both cellulose and sucrose, along with a minor increase in the production of 6-membered all-carbon rings at 2200 K. During the carbonization of PET, the production of 6-membered all-carbon rings stabilizes over time regardless of temperature. Regarding the 5 and 7-membered all-carbon rings for PET, the observed range for carbon atom conversion ratios falls between 0.05 and 0.20 at 2600 K and between 0.00 and 0.10 at 2200 K.

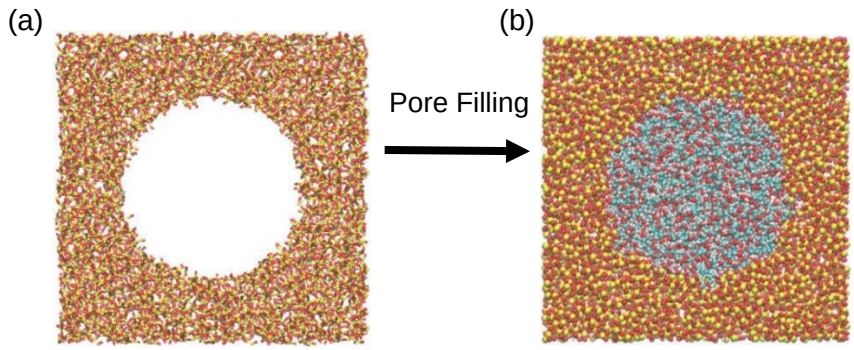

Figure 6: Mesoporous silica pore of 4 nm diameter (a) before and (b) after filling with carbon precursors.

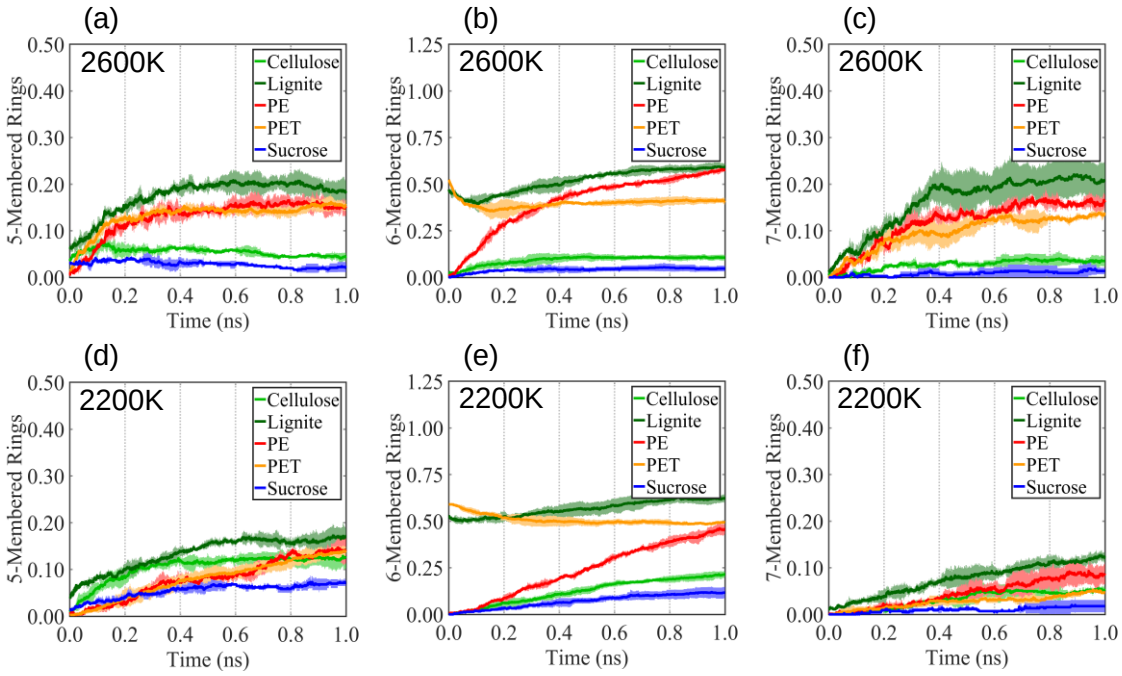

Figure 7: Formation of all-carbon rings during the carbonization process for various polymer precursors. The carbon atom conversion ratios of (a) 5-membered, (b) 6-membered, and (c) 7-membered all-carbon rings are presented for cellulose, lignite, PE, PET, and sucrose carbonized

at 2600 K. Additionally, the carbon atom conversion ratios of (d) 5-membered, (e) 6-membered, and (f) 7-membered all-carbon rings are displayed for cellulose, lignite, PE, PET, and sucrose carbonized at 2200 K.

3.5.Gaseous product formation analysis

Carbonization leads to the significant release of gaseous products, and as a result, the mesoporous silica pores need to be cleared intermittently. Here, we quantify the gaseous products mainly based on C_0, C_1 and C_2 carbon products. The C_0 products consist of gases without carbon, primarily comprising water vapor and hydrogen. C_1 consists of gases containing one carbon atom in compounds such as CO and CH_4, while C_2 comprises gases containing two carbon atoms, as found in compounds like C_2H_4. The quantification of the diverse gaseous products released by each of the polymer precursors is conducted on a per-molecule basis, as the number of molecules of each polymer used for the carbonization process are different. **Fig. 8** and **Fig. S2** represent the number of gaseous molecules of products formed by carbonizing each polymer at 2200 K and 2600 K. The performance of the polymer is evaluated based on the amount of gas released. A lower amount of gas release indicates a higher carbon yield or a greater presence of condensed phase carbon, as it increases the chances of formation of tar materials which are classified among the C_5, C_6 and C_7 aromatic structures. The tar components of the precursor settle on the inner surface of the silica pore and are good blocking agents for unreacted silica precursors. We find that polymer precursors containing oxygen in their structure yield a higher production of carbon monoxide and water vapor. Among the five polymers examined, cellulose exhibits the highest production of CO and H_2O, followed by PET. Polymers with O-containing groups like cellulose, PET, and sucrose decay faster than those without O-containing groups like PE. Hydroxyl groups remain longer than bridging ether links and carbonyl groups as the carbonization is initiated. This aligns with our earlier

theoretical investigations on the transformation of carbon fibers from diverse precursors [90,91] as well as the experimental findings [92,93] that the thermodynamic decomposition products mostly contain hydroxyl groups, since bridging ether links and carbonyl groups are less thermally stable. Apart from CO and H_2O, the gases released are saturated alcohols, methane, ethane, and propane. The gaseous products formed by carbonizing PE are H_2, CH_4, C_2H_4 and C_3H_6 mostly. At 2600 K, we find that the production of gases increases, which means that the precursors decay faster. The production of gases like H_2 increases (see **Fig. S2d**), which means that a significant portion of the carbon has been converted into graphitic or turbostratic structures. At 2200 K, we observe a significant portion of the carbon gets converted to CH_4, C_2H_4 and C_3H_6 gaseous species. We widely accept that 2600 K is a more optimal temperature for carbonization compared to 2200 K, as it promotes the formation of desired carbon structures.

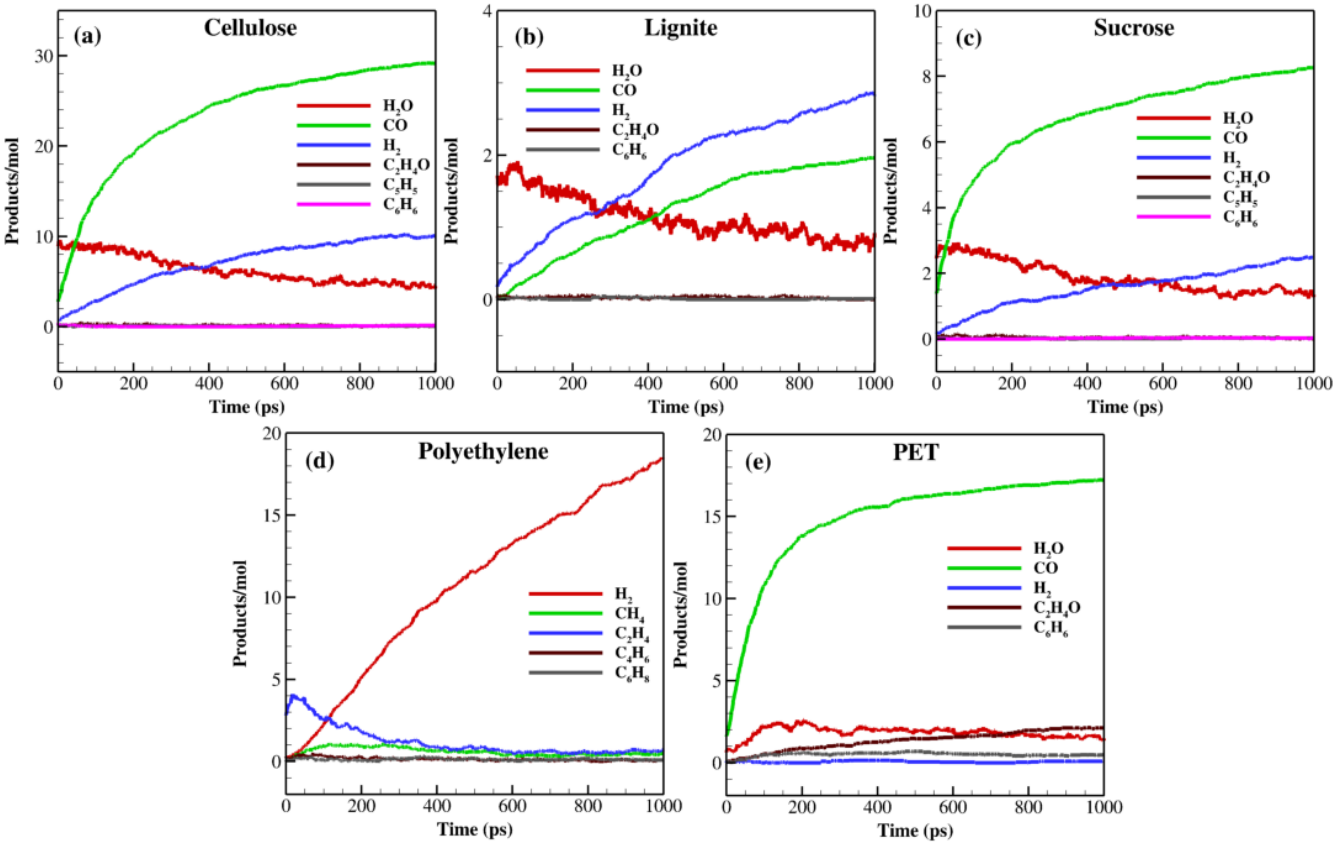

Figure 8: Production of gaseous species, normalized to number of gases per precursor molecule, during the carbonization of carbon precursors, (a) cellulose, (b) lignite, (c) sucrose, (d) PE, and (e) PET at 2200 K.

3.6.Hybridization

We calculate the hybridization of each carbon atom present within the polymer over the time evolution of carbonization process. The hybridization is classified based on sp^3 and sp^2 carbon at two different temperatures. Hybridization reveals whether a carbon atom lies on a plane with neighboring carbon atoms or not. Generally, planar carbon atoms are part of the 6-membered all-carbon rings, while curvature and the bridging sections of turbostratic graphene or graphitic structures are attributed to the presence of 5- and 7-membered all-carbon rings. They comprise of

tar products formed from carbonization and are sp^2 hybridized. Other products formed during the process typically consist of gases, which may or may not include sp^3 hybridized carbon. Unsaturated char components like alcohol, aldehydes, and ketones, which are formed from further degradation of materials, are sp^3 hybridized in nature.

We calculate the time evolution of sp^3 and sp^2 hybridized carbon atoms per molecule of each polymer. The criteria whether a particular carbon atom is sp^2 is to find the neighboring atoms and check whether all the atoms forming the connection are within 10 % of the same plane or not. **Fig. 9** illustrates the evolution of carbon atom hybridization as five polymer precursors undergo carbonization at both 2200 K and 2600 K. We observe that the evolution of sp^2 hybridized carbon correlates with the ring analysis conducted earlier. Furthermore, we note that the decline in sp^2 hybridized carbon stabilizes more rapidly at 2600 K than at 2200 K. This indicates that the turbostratic graphene structures formed at 2600 K remain largely intact for an extended duration. However, the char components formed eventually undergo further fragmentation, leading to the generation of gaseous components that are unsuitable for carbonization. Substantial layers of carbon fibers can be obtained through prolonged carbonization at high temperature. From the hybridization analysis, carbonization of PE primarily leads to the formation of planar (sp^2) structures, while carbonization of sucrose yields structures that are the least planar. **Fig. 10** shows the snapshot of formation of turbostratic graphene structures within PE and sucrose which echoes the hybridization analysis. **Fig. S3** provides snapshots of formation of aromatic ring structures from other carbon precursors. The graphitic structures inside the silica pore serve as thick layers of tar which act as protective coatings against unreacted silicic acid.

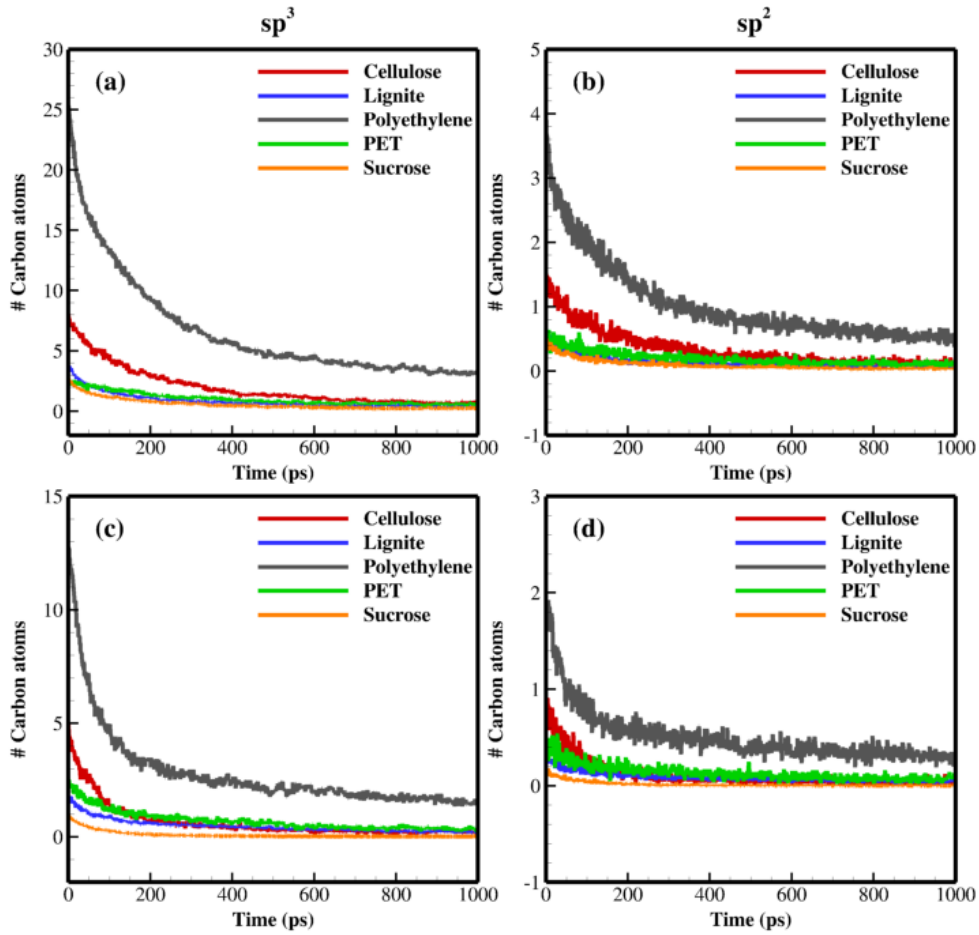

Figure 9: Evolution of hybridization for the five polymer precursors carbonized at 2200 K, showing (a) sp^3 and (b) sp^2 carbon atoms; and carbonized at 2600 K, showing (c) sp^3 and (d) sp^2 carbon atoms.

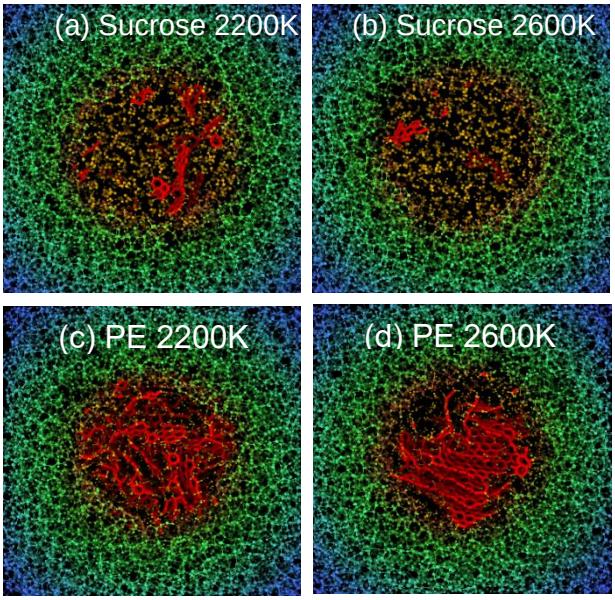

Figure 10: Formation of turbostratic graphene structures during the carbonization for (a) sucrose at 2200 K, (b) sucrose at 2600 K, (c) PE at 2200 K, and (d) PE at 2600 K.

3.7.Interaction of carbonaceous tar with unreacted silica precursors

To analyze the resistance of turbostratic graphene structures, we studied the dynamics of silicic acid precursors inside the MSM nanopore. Upon quenching the silica nanopore along with carbonized products back to ambient condition, we obtain the deposition of thick tar layers on the inner surface of the silica pore, as shown in **Fig. 11**a. After removing the unwanted gaseous products and char products from the silica nanopore, we find the deposition of tar products on the surface of the silica pore. To assess the efficacy of these tar coatings in preventing unreacted silicic acid from interacting with the small pore surfaces, we introduce an unreacted silicic acid molecule into the pore space, as shown in **Fig. 11**b. We consider a PET turbostratic graphene structure in a silica nanopore formed at 2600 K as the tar components to study the protective blocking of unreacted silicic acid precursor. The trajectory of the unreacted silicic acid has been tracked at

each timestep of the MD simulation at 300 K. We plot the trajectory of the unreacted silicic acid precursor inside the pore space in **Fig. 11**c. The trajectory reveals that silicic acid never crosses the barrier formed by the tar coating of the PET-derived carbon structures inside the pore (see **Fig. 11**c). As such, we can safely infer that the surface of the silica is adequately coated with PET tar effectively preventing unreacted silicic acid from interacting with the inner silica pore surface. The mesoporous silica structures are often coated with monodispersed protective layers of polymers to form core shell particles [94]. The carbonized polymers provide protection for the inner surface of the MSM nanopore, shielding it from exposure to silica precursors during the assembly step. This precautionary measure prevents potential damage to the small pores in MSMs.

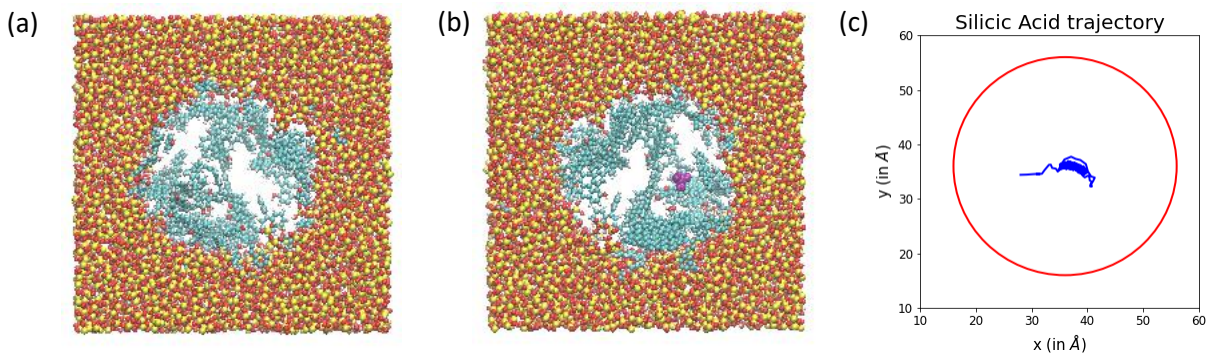

Figure 11: (a) Quenching and cleaning of gaseous compounds from silica mesopores, (b) introduction of unreacted silicic acid precursor (colored in purple) inside the pore, and (c) trajectory of silicic acid precursor inside the pore.

4. Conclusions

We develop a facile computational strategy combining non-reactive and reactive molecular dynamics (MD) simulations to synthesize and heal mesoporous silica materials (MSMs). The early stages of the self-assembly of pluronic polymers is delineated from MD simulations performed by

non-reactive OPLS-AA force field. Our simulations indicate a distinct segregation between the hydrophilic and hydrophobic part of the pluronic polymer. The condensation of silica precursors around the micelle structure is studied using the accelerated bond-boosted ReaxFF simulations, which yields the silica network on the micelle structure with subsequent dehydration. This step is important for the templating of mesoporous silica structures. We observe that over 60 % of the silicic acid precursors undergo condensation during our simulation, with higher temperatures significantly accelerating the condensation rate. The post synthesis healing of silica mesopores is performed by carbonizing five polymer precursors inside the pores using the ReaxFF MD simulations. The formation of turbostratic graphene structures is observed mainly from linear chain polyethylene and aromatic lignite. To test the protective efficacy of the carbonized polymer coating on nanopore, we disperse a few silica precursors, effectively preventing them from interacting with the surface. Our findings indicate that the coating successfully shields the pore from the silica precursors.

Our investigation on the carbonization of polymers inside the silica nanopore opens door for new methods of functionalization of MSMs. Mesoporous spherical particles can be modified with a great variety of functionalities for sensing applications. Carbon coatings can enhance pore properties, in addition to protecting the inner surface of the pores from damage. Remarkable properties of carbon fibers such as high modulus and tensile strength can increase the durability of MSMs when functionalized. Nitrogen containing polymers are good absorbers for gases, such as carbon dioxide, making MSMs suitable materials for separation. Moreover, the integration of carbon coatings into MSMs presents a promising avenue for future advancements in fields such as anticorrosion, sensing, and biomedical applications.

Acknowledgement

We acknowledge funding support from the Multi-Scale Fluid-Solid Interactions in Architected and Natural Materials (MUSE) Center, an Energy Frontier Research Center funded by the U.S. Department of Energy (DOE), Office of Science, Basic Energy Science.

References

[1] B.J. Melde, B.J. Johnson, P.T. Charles, Mesoporous Silicate Materials in Sensing, Sensors. 8 (2008) 5202–5228.

[2] A. Llopis-Lorente, B. Lozano-Torres, A. Bernardos, R. Martínez-Máñez, F. Sancenón, Mesoporous silica materials for controlled delivery based on enzymes, J. Mater. Chem. B. 5 (2017) 3069–3083.

[3] T. Asefa, Z. Tao, Mesoporous silica and organosilica materials—Review of their synthesis and organic functionalization, Can. J. Chem. 90 (2012) 1015–1031.

[4] S. Kumar, M.M. Malik, R. Purohit, Synthesis Methods of Mesoporous Silica Materials, Mater. Today Proc. 4 (2017) 350–357.

[5] M. A., S. F., H. Q., K. D., M. D., M.R. S., S.G. D., K. M., P. P., F. A., J. M., C.B. F., Cooperative Formation of Inorganic-Organic Interfaces in the Synthesis of Silicate Mesostructures, Science (80-.). 261 (1993) 1299–1303.

[6] J.S. Beck, J.C. Vartuli, W.J. Roth, M.E. Leonowicz, C.T. Kresge, K.D. Schmitt, C.T.W. Chu, D.H. Olson, E.W. Sheppard, S.B. McCullen, J.B. Higgins, J.L. Schlenker, A new family of mesoporous molecular sieves prepared with liquid crystal templates, J. Am. Chem. Soc. 114 (1992) 10834–10843.

[7] S. Savic, K. Vojisavljevic, M. Počuča-Nešić, K. Zivojevic, M. Mladenovic, N. Knezevic, Hard Template Synthesis of Nanomaterials Based on Mesoporous Silica, Metall. Mater. Eng. 24 (2018).

[8] D. Al Husseini, Y. Karanth, J. Zhou, D. Willhelm, X. Qian, R. Gutierrez-Osuna, G.L. Coté, P.T. Lin, S.A. Sukhishvili, Surface Functionalization Utilizing Mesoporous Silica Nanoparticles for Enhanced Evanescent-Field Mid-Infrared Waveguide Gas Sensing, Coatings. 11 (2021).

[9] D.R. Radu, C.-Y. Lai, J.W. Wiench, M. Pruski, V.S.-Y. Lin, Gatekeeping Layer Effect: A Poly(lactic acid)-coated Mesoporous Silica Nanosphere-Based Fluorescence Probe for Detection of Amino-Containing Neurotransmitters, J. Am. Chem. Soc. 126 (2004) 1640–1641.

[10] T.M. Budnyak, S. Modersitzki, I. V Pylypchuk, J. Piątek, A. Jaworski, O. Sevastyanova, M.E. Lindström, A. Slabon, Tailored Hydrophobic/Hydrophilic Lignin Coatings on Mesoporous Silica for Sustainable Cobalt(II) Recycling, ACS Sustain. Chem. Eng. 8 (2020) 16262–16273.

[11] E.J. Park, Y.K. Cho, D.H. Kim, M.-G. Jeong, Y.H. Kim, Y.D. Kim, Hydrophobic Polydimethylsiloxane (PDMS) Coating of Mesoporous Silica and Its Use as a Preconcentrating Agent of Gas Analytes, Langmuir. 30 (2014) 10256–10262.

[12] L.M. Henning, U. Simon, A. Gurlo, G.J. Smales, M.F. Bekheet, Grafting and stabilization of ordered mesoporous silica COK-12 with graphene oxide for enhanced removal of methylene blue, RSC Adv. 9 (2019) 36271–36284.

[13] T. Kwon, H. Nishihara, Y. Fukura, K. Inde, N. Setoyama, Y. Fukushima, T. Kyotani,

Carbon-coated mesoporous silica as an electrode material, Microporous Mesoporous Mater. 132 (2010) 421–427.

[14] L. Li, Y. Sun, B. Cao, H. Song, Q. Xiao, W. Yi, Preparation and performance of polyurethane/mesoporous silica composites for coated urea, Mater. Des. 99 (2016) 21–25.

[15] S. V Lamaka, D.G. Shchukin, D. V Andreeva, M.L. Zheludkevich, H. Möhwald, M.G.S. Ferreira, Sol-Gel/Polyelectrolyte Active Corrosion Protection System, Adv. Funct. Mater. 18 (2008) 3137–3147.

[16] E. Albert, N. Cotolan, N. Nagy, G. Sáfrán, G. Szabó, L.-M. Mureşan, Z. Hórvölgyi, Mesoporous silica coatings with improved corrosion protection properties, Microporous Mesoporous Mater. 206 (2015) 102–113.

[17] Y. Yin, H. Zhao, M. Prabhakar, M. Rohwerder, Organic composite coatings containing mesoporous silica particles: Degradation of the SiO2 leading to self-healing of the delaminated interface, Corros. Sci. 200 (2022) 110252.

[18] F. Olivieri, R. Castaldo, M. Cocca, G. Gentile, M. Lavorgna, Mesoporous silica nanoparticles as carriers of active agents for smart anticorrosive organic coatings: a critical review, Nanoscale. 13 (2021) 9091–9111.

[19] B. Židov, Z. Lin, I. Stojanović, L. Xu, Impact of inhibitor loaded mesoporous silica nanoparticles on waterborne coating performance in various corrosive environments, J. Appl. Polym. Sci. 138 (2021) 49614.

[20] J.M. Falcón, L.M. Otubo, I. V Aoki, Highly ordered mesoporous silica loaded with dodecylamine for smart anticorrosion coatings, Surf. Coatings Technol. 303 (2016) 319–

329.

[21] X. Li, X. Du, J. He, Self-Cleaning Antireflective Coatings Assembled from Peculiar Mesoporous Silica Nanoparticles, Langmuir. 26 (2010) 13528–13534.

[22] Y. Zhang, C.Y. Ang, M. Li, S.Y. Tan, Q. Qu, Z. Luo, Y. Zhao, Polymer-Coated Hollow Mesoporous Silica Nanoparticles for Triple-Responsive Drug Delivery, ACS Appl. Mater. Interfaces. 7 (2015) 18179–18187.

[23] F. Gao, H. Zhou, Z. Shen, G. Zhu, L. Hao, H. Chen, H. Xu, X. Zhou, Long-lasting anti-bacterial activity and bacteriostatic mechanism of tea tree oil adsorbed on the amino-functionalized mesoporous silica-coated by PAA, Colloids Surfaces B Biointerfaces. 188 (2020) 110784.

[24] B. Chang, X. Sha, J. Guo, Y. Jiao, C. Wang, W. Yang, Thermo and pH dual responsive, polymer shell coated, magnetic mesoporous silica nanoparticles for controlled drug release, J. Mater. Chem. 21 (2011) 9239–9247.

[25] B. Dumontel, V. Conejo-Rodríguez, M. Vallet-Regí, M. Manzano, Natural Biopolymers as Smart Coating Materials of Mesoporous Silica Nanoparticles for Drug Delivery, Pharmaceutics. 15 (2023).

[26] N. Ehlert, M. Badar, A. Christel, S.J. Lohmeier, T. Luessenhop, M. Stieve, T. Lenarz, P.P. Mueller, P. Behrens, Mesoporous silica coatings for controlled release of the antibiotic ciprofloxacin from implants, J. Mater. Chem. 21 (2011) 752–760.

[27] S. Bhattacharyya, H. Wang, P. Ducheyne, Polymer-coated mesoporous silica nanoparticles for the controlled release of macromolecules, Acta Biomater. 8 (2012) 3429–3435.

[28] X. Yang, P. Qiu, J. Yang, Y. Fan, L. Wang, W. Jiang, X. Cheng, Y. Deng, W. Luo, Mesoporous Materials–Based Electrochemical Biosensors from Enzymatic to Nonenzymatic, Small. 1904022 (2019) 1–16.

[29] J.-K. Wang, Q. Zhou, J.-P. Wang, S. Yang, G.L. Li, Hydrophobic self-healing polymer coatings from carboxylic acid- and fluorine-containing polymer nanocontainers, Colloids Surfaces A Physicochem. Eng. Asp. 569 (2019) 52–58.

[30] K. Alipour, F. Nasirpouri, Smart anti-corrosion self-healing zinc metal-based molybdate functionalized-mesoporous-silica (MCM-41) nanocomposite coatings, RSC Adv. 7 (2017) 51879–51887.

[31] L. Xiong, J. Liu, Y. Li, S. Li, M. Yu, Enhancing corrosion protection properties of sol-gel coating by pH-responsive amino-silane functionalized graphene oxide-mesoporous silica nanosheets, Prog. Org. Coatings. 135 (2019) 228–239.

[32] P. Du, J. Wang, H. Zhao, G. Liu, L. Wang, Graphene oxide encapsulated by mesoporous silica for intelligent anticorrosive coating: studies on release models and self-healing ability, Dalt. Trans. 48 (2019) 13064–13073.

[33] C. Feng, L. Zhu, K. Cao, Z. Yu, Y. Song, Difunctional Silicon Dioxide Combined with Graphene Oxide Nanocomposite to Enhance the Anticorrosion Performance of Epoxy Coatings, ACS Omega. 7 (2022) 24134–24144.

[34] A. Farooq, A. Shukur, C. Astley, L. Tosheva, P. Kelly, D. Whitehead, M. Azzawi, Titania coating of mesoporous silica nanoparticles for improved biocompatibility and drug release within blood vessels, Acta Biomater. 76 (2018) 208–216.

[35] D.G. Shchukin, H. Möhwald, Smart nanocontainers as depot media for feedback active coatings, Chem. Commun. 47 (2011) 8730–8739.

[36] X. Sun, W. Yu, J. Yan, J. Li, G. Jin, J. Feng, Z. Guo, X. Liang, Mesoporous silica–carbon composites fabricated by a universal strategy of hydrothermal carbonization: controllable synthesis and applications, RSC Adv. 8 (2018) 27207–27215.

[37] C.-Y. Chen, H.-X. Li, M.E. Davis, Studies on mesoporous materials: I. Synthesis and characterization of MCM-41, Microporous Mater. 2 (1993) 17–26.

[38] G.S. Attard, J.C. Glyde, C.G. Göltner, Liquid-crystalline phases as templates for the synthesis of mesoporous silica, Nature. 378 (1995) 366–368.

[39] P. Yang, D. Zhao, B.F. Chmelka, G.D. Stucky, Triblock-Copolymer-Directed Syntheses of Large-Pore Mesoporous Silica Fibers, Chem. Mater. 10 (1998) 2033–2036.

[40] M.E. Davis, Ordered porous materials for emerging applications, Nature. 417 (2002) 813–821.

[41] Z.-A. Qiao, L. Zhang, M. Guo, Y. Liu, Q. Huo, Synthesis of Mesoporous Silica Nanoparticles via Controlled Hydrolysis and Condensation of Silicon Alkoxide, Chem. Mater. 21 (2009) 3823–3829.

[42] Q. Huo, D.I. Margolese, G.D. Stucky, Surfactant Control of Phases in the Synthesis of Mesoporous Silica-Based Materials, Chem. Mater. 8 (1996) 1147–1160.

[43] F.R. Siperstein, K.E. Gubbins, Synthesis and Characterization of Templated Mesoporous Materials Using Molecular Simulation, Mol. Simul. 27 (2001) 339–352.

[44] F.R. Siperstein, K.E. Gubbins, Phase Separation and Liquid Crystal Self-Assembly in

Surfactant−Inorganic−Solvent Systems, Langmuir. 19 (2003) 2049–2057.

[45] A. Patti, A.D. Mackie, F.R. Siperstein, Monte Carlo Simulation of Self-Assembled Ordered Hybrid Materials, Langmuir. 23 (2007) 6771–6780.

[46] A. Patti, F.R. Siperstein, A.D. Mackie, Phase Behavior of Model Surfactants in the Presence of Hybrid Particles, J. Phys. Chem. C. 111 (2007) 16035–16044.

[47] A. Patti, A.D. Mackie, V. Zelenak, F.R. Siperstein, One-pot synthesis of amino functionalized mesoporous silica materials: using simulations to understand transitions between different structures, J. Mater. Chem. 19 (2009) 724–732.

[48] A. Patti, A.D. Mackie, F.R. Siperstein, Monte Carlo simulations of self-assembling hexagonal and cage-like bifunctional periodic mesoporous materials, J. Mater. Chem. 19 (2009) 7848–7855.

[49] C. Schumacher, J. Gonzalez, P.A. Wright, N.A. Seaton, Generation of Atomistic Models of Periodic Mesoporous Silica by Kinetic Monte Carlo Simulation of the Synthesis of the Material, J. Phys. Chem. B. 110 (2006) 319–333.

[50] L. Jin, S.M. Auerbach, P.A. Monson, Simulating the Formation of Surfactant-Templated Mesoporous Silica Materials: A Model with Both Surfactant Self-Assembly and Silica Polymerization, Langmuir. 29 (2013) 766–780.

[51] A. Centi, M. Jorge, Molecular Simulation Study of the Early Stages of Formation of Bioinspired Mesoporous Silica Materials, Langmuir. 32 (2016) 7228–7240.

[52] S.-C. Chien, G. Pérez-Sánchez, J.R.B. Gomes, M.N.D.S. Cordeiro, M. Jorge, S.M. Auerbach, P.A. Monson, Molecular Simulations of the Synthesis of Periodic Mesoporous

Silica Phases at High Surfactant Concentrations, J. Phys. Chem. C. 121 (2017) 4564–4575.

[53] W.L. Jorgensen, D.S. Maxwell, J. Tirado-Rives, Development and Testing of the OPLS All-Atom Force Field on Conformational Energetics and Properties of Organic Liquids, J. Am. Chem. Soc. 118 (1996) 11225–11236.

[54] M. Matsui, A transferable interatomic potential model for crystals and melts in the system Cao-MgO-Al_2O_3-SiO_2, Miner. Mag. 58 (1994) 571–572.

[55] R.T. Cygan, J.-J. Liang, A.G. Kalinichev, Molecular Models of Hydroxide, Oxyhydroxide, and Clay Phases and the Development of a General Force Field, J. Phys. Chem. B. 108 (2004) 1255–1266.

[56] P. Mark, L. Nilsson, Structure and Dynamics of the TIP3P, SPC, and SPC/E Water Models at 298 K, J. Phys. Chem. A. 105 (2001) 9954–9960.

[57] A. Bródka, T.W. Zerda, Properties of liquid acetone in silica pores: Molecular dynamics simulation, J. Chem. Phys. 104 (1996) 6319–6326.

[58] I.C. Bourg, C.I. Steefel, Molecular Dynamics Simulations of Water Structure and Diffusion in Silica Nanopores, J. Phys. Chem. C. 116 (2012) 11556–11564.

[59] B.P. Feuston, J.B. Higgins, Model Structures for MCM-41 Materials: A Molecular Dynamics Simulation, J. Phys. Chem. 98 (1994) 4459–4462.

[60] T.S. Gulmen, W.H. Thompson, Model silica pores with controllable surface chemistry for molecular dynamics simulatinos, MRS Online Proc. Libr. 899 (2006) 605.

[61] H. Kraus, J. Rybka, A. Höltzel, N. Trebel, U. Tallarek, N. Hansen, PoreMS: a software tool for generating silica pore models with user-defined surface functionalisation and pore

dimensions, Mol. Simul. 47 (2021) 306–316.

[62] A.C.T. van Duin, S. Dasgupta, F. Lorant, W.A. Goddard, ReaxFF: A Reactive Force Field for Hydrocarbons, J. Phys. Chem. A. 105 (2001) 9396–9409.

[63] T.P. Senftle, S. Hong, M.M. Islam, S.B. Kylasa, Y. Zheng, Y.K. Shin, C. Junkermeier, R. Engel-Herbert, M.J. Janik, H.M. Aktulga, T. Verstraelen, A. Grama, A.C.T. van Duin, The ReaxFF reactive force-field: development, applications and future directions, Npj Comput. Mater. 2 (2016) 15011.

[64] N. Dasgupta, Y. Kyung Shin, M. V Fedkin, A.C.T. van Duin, ReaxFF molecular dynamics simulations on the structure and dynamics of electrolyte water systems at ambient temperature, Comput. Mater. Sci. 172 (2020) 109349.

[65] Y. Gao, W. Zhu, T. Wang, D.E. Yilmaz, A.C.T. van Duin, C/H/O/F/Al ReaxFF Force Field Development and Application to Study the Condensed-Phase Poly(vinylidene fluoride) and Reaction Mechanisms with Aluminum, J. Phys. Chem. C. 126 (2022) 11058–11074.

[66] S.H. Hahn, A.C.T. van Duin, Surface Reactivity and Leaching of a Sodium Silicate Glass Under Aqueous Environment: A ReaxFF Molecular Dynamics Study, J. Phys. Chem. C. (2019).

[67] M.M. Islam, C. Zou, A.C.T. van Duin, S. Raman, Interactions of hydrogen with the iron and iron carbide interfaces: a ReaxFF molecular dynamics study, Phys. Chem. Chem. Phys. 18 (2016) 761–771.

[68] N. Dasgupta, C. Chen, A.C.T. van Duin, Development and application of ReaxFF methodology for understanding the chemical dynamics of metal carbonates in aqueous

solutions, Phys. Chem. Chem. Phys. 24 (2022) 3322–3337.

[69] K. Ganeshan, M.J. Hossain, A.C.T. van Duin, Multiply accelerated ReaxFF molecular dynamics: coupling parallel replica dynamics with collective variable hyper dynamics, Mol. Simul. 45 (2019) 1265–1272.

[70] N. Dasgupta, T.A. Ho, S.B. Rempe, Y. Wang, Hydrophobic Nanoconfinement Enhances CO2 Conversion to H2CO3, J. Phys. Chem. Lett. 14 (2023) 1693–1701.

[71] A. Vashisth, C. Ashraf, W. Zhang, C.E. Bakis, A.C.T. van Duin, Accelerated ReaxFF Simulations for Describing the Reactive Cross-Linking of Polymers, J. Phys. Chem. A. 122 (2018) 6633–6642.

[72] Z. Jing, L. Xin, H. Sun, Replica exchange reactive molecular dynamics simulations of initial reactions in zeolite synthesis, Phys. Chem. Chem. Phys. 17 (2015) 25421–25428.

[73] E. Apol, R. Apostolov, H. Berendsen, A. Buuren, P. Bjelkmar, R. Drunen, K.A. Feenstra, S. Fritsch, G. Groenhof, C. Junghans, P. Kasson, P. Larsson, P. Meulenhoff, T. Murtola, S. Pall, S. Pronk, R. Schulz, M. Shirts, A. Sijbers, E. Lindahl, Gromacs User Manual Version 4.6, 2013.

[74] H.J.C. Berendsen, J.R. Grigera, T.P. Straatsma, The missing term in effective pair potentials, J. Phys. Chem. 91 (1987) 6269–6271.

[75] S. Nosé, A molecular dynamics method for simulations in the canonical ensemble, Mol. Phys. 52 (1984) 255–268.

[76] M. Parrinello, A. Rahman, Polymorphic transitions in single crystals: A new molecular dynamics method, J. Appl. Phys. 52 (1981) 7182–7190.

[77] R.W. Hockney, S.P. Goel, J.W. Eastwood, Quiet high-resolution computer models of a plasma, J. Comput. Phys. 14 (1974) 148–158.

[78] M.C. Pitman, A.C.T. van Duin, Dynamics of Confined Reactive Water in Smectite Clay–Zeolite Composites, J. Am. Chem. Soc. 134 (2012) 3042–3053.

[79] H.J.C. Berendsen, J.P.M. Postma, W.F. van Gunsteren, A. DiNola, J.R. Haak, Molecular dynamics with coupling to an external bath, J. Chem. Phys. 81 (1984) 3684–3690.

[80] N. Dasgupta, D.E. Yilmaz, A. van Duin, Simulations of the Biodegradation of Citrate-Based Polymers for Artificial Scaffolds Using Accelerated Reactive Molecular Dynamics, J. Phys. Chem. B. 124 (2020) 5311–5322.

[81] E.J. Baerends, T. Ziegler, A.J. Atkins, J. Autschbach, D. Bashford, O. Baseggio, A. Bérces, F.M. Bickelhaupt, C. Bo, P.M. Boerritger, L. Cavallo, C. Daul, D.P. Chong, D. V Chulhai, L. Deng, R.M. Dickson, J.M. Dieterich, D.E. Ellis, M. van Faassen, A. Ghysels, A. Giammona, S.J.A. van Gisbergen, A. Goez, A.W. Götz, S. Gusarov, F.E. Harris, P. van den Hoek, Z. Hu, C.R. Jacob, H. Jacobsen, L. Jensen, L. Joubert, J.W. Kaminski, G. van Kessel, C. König, F. Kootstra, A. Kovalenko, M. Krykunov, E. van Lenthe, D.A. McCormack, A. Michalak, M. Mitoraj, S.M. Morton, J. Neugebauer, V.P. Nicu, L. Noodleman, V.P. Osinga, S. Patchkovskii, M. Pavanello, C.A. Peeples, P.H.T. Philipsen, D. Post, C.C. Pye, H. Ramanantoanina, P. Ramos, W. Ravenek, J.I. Rodríguez, P. Ros, R. Rüger, P.R.T. Schipper, D. Schlüns, H. van Schoot, G. Schreckenbach, J.S. Seldenthuis, M. Seth, J.G. Snijders, M. Solà, S. M., M. Swart, D. Swerhone, G. te Velde, V. Tognetti, P. Vernooijs, L. Versluis, L. Visscher, O. Visser, F. Wang, T.A. Wesolowski, E.M. van Wezenbeek, G. Wiesenekker, S.K. Wolff, T.K. Woo, A.L. Yakovlev, ADF2017, SCM, Theoretical Chemistry, Vrije

Universiteit, Amsterdam, The Netherlands,

[82] S. Kerkhofs, T. Willhammar, H. Van Den Noortgate, C.E.A. Kirschhock, E. Breynaert, G. Van Tendeloo, S. Bals, J.A. Martens, Self-Assembly of Pluronic F127—Silica Spherical Core–Shell Nanoparticles in Cubic Close-Packed Structures, Chem. Mater. 27 (2015) 5161–5169.

[83] S.H. Hahn, J. Rimsza, L. Criscenti, W. Sun, L. Deng, J. Du, T. Liang, S.B. Sinnott, A.C.T. Van Duin, Development of a ReaxFF reactive force field for NaSiO x/water systems and its application to sodium and proton self-diffusion, J. Phys. Chem. C. 122 (2018) 19613–19624.

[84] Y. Sun, K. Ma, T. Kao, K.A. Spoth, H. Sai, D. Zhang, L.F. Kourkoutis, V. Elser, U. Wiesner, Formation pathways of mesoporous silica nanoparticles with dodecagonal tiling, Nat. Commun. 8 (2017) 252.

[85] D.A. Crerar, E. V Axtmann, R.C. Axtmann, Growth and ripening of silica polymers in aqueous solutions, Geochim. Cosmochim. Acta. 45 (1981) 1259–1266.

[86] D.J. Belton, O. Deschaume, C.C. Perry, An overview of the fundamentals of the chemistry of silica with relevance to biosilicification and technological advances, FEBS J. 279 (2012) 1710–1720.

[87] M. Jorge, J.R.B. Gomes, M.N.D.S. Cordeiro, N.A. Seaton, Molecular Dynamics Simulation of the Early Stages of the Synthesis of Periodic Mesoporous Silica, J. Phys. Chem. B. 113 (2009) 708–718.

[88] A.C. Makrides, M. Turner, J. Slaughter, Condensation of silica from supersaturated silicic

acid solutions, J. Colloid Interface Sci. 73 (1980) 345–367.

[89] T. Du, H. Li, G. Sant, M. Bauchy, New insights into the sol–gel condensation of silica by reactive molecular dynamics simulations, J. Chem. Phys. 148 (2018) 234504.

[90] Q. Mao, S. Rajabpour, M.K. Talkhoncheh, J. Zhu, M. Kowalik, A.C.T. van Duin, Cost-effective carbon fiber precursor selections of polyacrylonitrile-derived blend polymers: carbonization chemistry and structural characterizations, Nanoscale. 14 (2022) 6357–6372.

[91] Q. Mao, S. Rajabpour, M. Kowalik, A.C.T. van Duin, Predicting cost-effective carbon fiber precursors: Unraveling the functionalities of oxygen and nitrogen-containing groups during carbonization from ReaxFF simulations, Carbon N. Y. 159 (2020) 25–36.

[92] J.N. Hay, D.J. Kemmish, Thermal decomposition of poly(aryl ether ketones), Polymer (Guildf). 28 (1987) 2047–2051.

[93] P. Patel, T.R. Hull, R.W. McCabe, D. Flath, J. Grasmeder, M. Percy, Mechanism of thermal decomposition of poly(ether ether ketone) (PEEK) from a review of decomposition studies, Polym. Degrad. Stab. 95 (2010) 709–718.

[94] F. Li, A. Stein, Functional Composite Membranes Based on Mesoporous Silica Spheres in a Hierarchically Porous Matrix, Chem. Mater. 22 (2010) 3790–3797.